9/26/02

Evidence for Transverse Dependencies in COTR and Microbunching in a SASE FEL*

A. H. Lumpkin, Y.C. Chae, J. W. Lewellen, W. J. Berg, M. Borland, S. G. Biedron, R. J. Dejus, M. Erdmann, Z. Huang, K.–J. Kim, Y. Li, S. V. Milton, E. R. Moog, D. W. Rule[+], V. Sajaev, B. X. Yang

Advanced Photon Source, Argonne National Laboratory, Argonne, IL 60439 USA

Abstract

Using coherent optical transition radiation (COTR) techniques, we have observed transverse dependencies, which in some aspects relate to the electron beam microbunching in a visible wavelength (540 nm) self-amplified spontaneous emission (SASE) free-electron laser (FEL). The experimental COTR observations include the z-dependent e-beam sizes, the z-dependent angular distributions, and the z-dependent spectra (which show an x-dependence). A 30-40% narrowing of the observed beam size using COTR is explainable by the mechanism's dependence on the square of the number of microbunched particles. However, additional effects are needed to explain beam size reductions by factors of 2-3 at different z locations. Localized e-beam structure in the gun or induced in the bunch compression process may result in microbunching transverse dependence, and hence the observed COTR effects.

[+]NSWC, Carderock Division, West Bethsda, MD

*Work supported by the U.S. Department of Energy, Office of Basic Energy Sciences under Contract No. W-31-109-ENG-38.

Introduction

The basic models of electron-beam microbunching in a self-amplified spontaneous emission (SASE) free-electron laser (FEL) describe the density modulation in the longitudinal distribution of the micropulse at the fundamental wavelength of the FEL [1-4]. While observation of the spectral enhancement in coherent transition radiation in a SASE FEL was reported at 13 μm [5], the actual observation of the variation of the modulation and microbunching fraction with peak current along the micropulse time profile has been observed only in an infrared oscillator experiment to date [6]. However, we have observed in our 540-nm wavelength SASE FEL transverse dependencies of coherent optical transition radiation (COTR), which in some aspects imply transverse microbunching phenomena [7,8]. In our measurements the longitudinal information is integrated by the detectors. Our experimental observations include the z-dependent e-beam sizes obtained by using a 500-nm short pass filter to select broadband OTR versus the narrow-band COTR emitted at 530 nm, the FEL fundamental. We can explain a 30-40% narrowing of the observed beam size using COTR by its intrinsic dependence on the square of the number of particles. However, additional effects are needed to explain the beam size reductions by factors of 2-3 at some z locations. Localized beam structure or an "effective core" in some parameters is predicted as a result of bunch compression in a chicane due to coherent synchrotron radiation (CSR) effects. Such a beam core would be reflected in the COTR intensity distributions. In addition to the near-field imaging, we report the complementary evidence from the far-field COTR interference images and the evidence from the imaging spectrometer for x-dependent spectra. Relevant information from GENESIS simulations and the ELEGANT particle tracking code are also discussed.

Experimental Background

The experiments were performed at the Advanced Photon Source (APS) low-energy undulator test line (LEUTL) facility [9]. A schematic of the facility is provided elsewhere in these proceedings [10]. These experiments used the photocathode (PC) rf gun, the S-band linac, the chicane bunch compressor [11], and the LEUTL hardware.

The diagnostic stations located before and after each station have been described previously [12]. For these experiments we used the 45° pick-off mirror at each station to direct the SASE radiation to the visible light detectors (VLDs) consisting of a CCD camera with up to three filter wheels. These filter wheels provided the appropriate bandpass (BP) filters and neutral density (ND) filters to keep the video signals out of saturation as one measures the dramatic z-dependent signal intensity growth due to the SASE process. Also, the 500-nm shortpass (SP) filters were installed at each station to sort OTR versus COTR signals. Both near-field and far-field imaging options were available via a remote-controlled translation stage that changed the camera-to-lens separation appropriately. For completeness, the schematic of the diagnostic station is shown in Fig. 1. The COTR experiments were performed by inserting the appropriate 6-μm-thick Al foil via the actuator 63 mm upstream of the 45° pick-off mirror. This foil both blocks the intense SASE light component and generates COTR for the interferometer experiments.

An additional capability involved the installation of a full set of mirror pairs and UV-visible lens pairs after each undulator. As seen in Fig. 2, a retractable mirror could be used to direct light into this transport optics and onto the Oriel M257 UV-visible spectrometer located in the tunnel. The lens pair was located at ~1.34 m from the in-

vacuum 45° mirror. The lenses had a separation of 36 mm at each station for 540–nm experiments. In practice this is an imaging spectrometer, so the 2-D information recorded by the readout camera involves wavelength on the horizontal axis and the x- or y-spatial profile on the vertical axis. For our optics we see the x-spatial profile. This system has been used to detect the production of sidebands [8] and the mode size change after SASE saturation, but it also was used to evaluate x–λ effects in the present experiments. An alignment laser beam at 543.5 nm wavelength was sent into the chamber bore in front of the first undulator, and the switching mirrors were used to verify light transport at all ten pick-off points. For a spectrometer entrance slit of 50 μm, a limiting resolution of ~0.9 nm (FWHM) was attained. The spectrometer functions were under EPICS control. By illumination of a 600-μm-diameter reference hole at the 45° mirror position, the optics was adjusted to center this feature in the entrance slit.

Experimental Results and Discussion

We now present results from the near-field imaging, far-field imaging and the spectrometer. We have previously reported what appeared to be effects on the transverse COTR intensities in beam size [13] and the far field [8], but for those experiments the 500-nm shortpass filters had not been installed in the filter wheels, so the sorting of OTR and COTR contributions at low gain was difficult.

Near Field Results

The near-field focus position of the camera/lens combination provides beam size and profile information. In our geometry we can evaluate electron beam information at the 45° mirror by eliminating the intense SASE light with the thin Al blocking foil located in the upstream actuator position at each station. The calibration factors for the VLD 1-8 stations were 80 μm/ch and 90 μm/ch for the x- and y-planes, respectively. We operated with a reduced peak current of 120 A (see Table 1) to limit the gain and the microbunching factor because we initially only had a single 500-nm shortpass filter available to attenuate by 100 the 530-540 nm fundamental COTR intensity. Examples of the z-dependent e-beam sizes are shown in Fig. 3. The upper figure shows the x-sizes in channels and the lower figure shows the y-sizes. For the VLD 5-8 stations, the data were taken as 100 images each with one 500-nm SP filter (OTR imaged, circles) and without this BP filter (COTR imaged, squares). In the latter case the appropriate ND filter was selected to keep the camera out of saturation. A dramatic measured beam size difference (> factor of 2) was observed between the OTR case and the COTR case at VLD 5. Systematically, the no-BP filter COTR case is smaller than the filtered case for the next three stations as well. As seen in Fig. 4, the integrated image intensities exhibit the exponential gain growth signature beginning at VLD 5. Both the SASE (upper) and COTR (lower) intensities show little gain (hence little microbunching) at VLD 1-4. (These gain curves also suggested an undulator alignment problem had developed with the settling of the concrete floor as subsequently verified by the survey team.) We have now taken some data with two shortpass filters in series at each station to improve the rejection of the microbunching component in the beam size measurement. These results

were consistent with our initial test, but allowed us to sort the COTR signals at even higher gains.

We have performed a calculation of the beam image spot narrowing that occurs when COTR is used as the conversion mechanism. If the bunching fraction is assumed to be uniform across the Gaussian–shaped transverse dimension, then the $(b_nN)^2$ term (where b_n is the microbunching factor for harmonic component n and N is the number of electrons in the micropulse) for the peak intensity will approximately give a $\sqrt{2}$ narrowing of the "observed" peak. In the GENESIS simulations [14] the bunching fraction is found to be uniform across the transverse dimensions for a time-slice sample when a smooth Gaussian e-beam distribution is used as input.

Far-Field Results

The camera-to-lens z separation can also be selected for far-field imaging. In this case the angular distribution patterns of the radiation are obtained. Based on the analytical model described in Ref. 15, the single-electron OTR interference (OTRI) pattern for two sources 63 mm apart is first calculated. This includes effects due to beam divergence. The calculated OTRI pattern exhibits fringes at $\theta = \pm 1.9, \pm 4.6, \pm 6.3$, and ± 7.5 mrad. The bunch form factor is multiplied times this pattern. Larger beam sizes (> 100 μm) have relatively narrow form factor functions in θ space. Figure 5 shows examples of the COTR fringe visibility variation with e-beam size. The COTR second fringe peaks are visible for beam sizes less than 50 μm, such as 25 μm in Fig. 5. The observed first fringe peak position varies with beam size for $\sigma > 100$ μm. An example of

an image is given in Fig. 4 of Ref. 8. In that case, the relative intensities of the fringe peaks implied σ_y = 30 μm with total divergences of 0.2 mrad (which would include the ~0.1 mrad scattering contribution from the Al foil). The σ_y = 30 μm result is smaller than the limiting resolution value of about one pixel at 90 μm/pixel for the near-field focus. As can be seen from Fig. 5, asymmetric beam sizes of σ_x = 100 μm and σ_y = 30 μm would give completely different fringe patterns in θ_x and θ_y. That is what was observed. In the case of the well-aligned FEL experiment previously reported [8], we noted the outer fringes were visible early in the gain process and in postsaturation, but not at saturation. These results are consistent with a beam core being initially involved in the microbunching. This core grows in transverse size up to saturation and then reduces to a residual core in the post saturation regime of this experiment. A debunching effect after the undulator regime that gives a residual core has been reported in an FEL amplifier experiment [16].

Imaging Spectrometer Results

The imaging spectrometer provides a complementary view of the situation. Due to the lower detection efficiency of this system, predominately COTR is seen since the broadband OTR is so much weaker. The microbunching fundamental wavelength is clearly evident in the x-λ images in Fig. 6 where the horizontal axis is wavelength and the vertical axis provides the x profile information. For the beam conditions given in Table 1 for the 300-A peak current, we clearly see structure in both dimensions in the x-λ image obtained after undulator 6. Most striking is the fact that the two spatial clusters separated by ~120 μm emit at two different wavelengths (2.9 nm apart). The beam size features in x are about 280 μm (FWHM) or σ_x = 120 μm. This is a factor of two lower than the

theoretical beam-matched value for β_x = 2.7 m and ε_x = 8 mm mrad. The complementary near-field measured x-beam size with VLD 6 was 240 μm (FWHM) averaged over 100 images. We have looked at ELEGANT simulation results of the beam after bunch compression in the chicane [17]. These simulations show some structure in the x distribution and some energy encoding in the bend plane, although this generally occurs at a higher compression than that of our 300-A case. Such a phenomena would be preferentially selected in the SASE process when higher 6-dimensional charge densities are involved. At some point the detailed experimentally determined distributions and/or ELEGANT-calculated distributions should be input to GENESIS to explore these effects.

Summary

In summary, we have discussed the growing evidence for transverse dependencies in the microbunching of electron beams in a SASE FEL. We have used complementary views into the beam distributions and intensity structure with near-field and far-field imaging coupled with the correlated x-λ views. We propose that the SASE FEL mechanism selectively interacts with the favorable cluster of beam induced in the chicane bunch compressor of our experiment. We also propose that the bunching fraction may vary within the electron beam transverse distribution during the exponential growth phase and in the debunching phase of our experiments.

Acknowledgements

The authors acknowledge the support of O. Singh, A. Rauchas, E. Gluskin, and R. Gerig of the APS.

References

1. Y. S. Derbenev, A. M. Kondratenko, and E. L. Saldin, Nucl. Instrum. Methods Phys. Res. 193, (1982) 452.

2. R. Bonifacio, C. Pellegrini, and L. Narducci, Opt. Commun. 50, (1984) 373.

3. K. –J. Kim, Nucl. Instrum. Methods Phys. Res. A250, (1986) 396.

4. J. –M. Wang and L. H. Yu, Nucl. Instrum. Methods Phys. Res. A250, (1986) 484.

5. A. Tremaine et al., Phys. Rev. Lett. 81, (1998) 5816.

6. Kenneth N. Ricci and Todd I. Smith, Phys. Rev. ST Accel. Beams 3, (2000) 032807-1.

7. A. H. Lumpkin et al., Phys. Rev. Lett. 86, (2001) 79.

8. A. H. Lumpkin et al., Phys. Rev. Lett. 88, (2002) 234801-1.

9. S. V. Milton et al., Nucl. Instrum. Methods Phys. Res., A407 (1998) 21.

10. A. H. Lumpkin et al., "Observations of z-Dependent Microbunching Harmonic Intensities using COTR in a SASE FEL," Nucl. Instrum. Meth. Phys. Res., these proceedings.

11. M. Borland, J. Lewellen, and S. V. Milton, Proceedings of the XX Linear Accelerator Conference (e Conf., Menlo Park, Ca 2000) 863 (2000).

12. E. Gluskin et al., Nucl. Instrum. Methods Phys. Res., A429, (1999) 358.

13. A. H. Lumpkin et al., "Advanced Intraundulator Electron Beam Diagnostics Using COTR Techniques," submitted to the Proceedings of the 10th Beam Instrumentation Workshop, Upton, NY, May 6-9, 2002.

14. S. Reiche, Nucl. Instrum. Methods Phys. Res., A429, (1999) 243.

15. D. W. Rule and A. H. Lumpkin, Proceedings of the 2001 Particle Accelerator Conference (IEEE, Piscataway, NJ, 2001), 1288.

16. J. Gardelle, J. Labrouche, and J.L. Rullier, Phys. Rev. Lett. 76, (1996) 4532.

17. M. Borland, "ELEGANT, A Flexible SDDS-Compliant Code for Accelerator Simulation," Advanced Photon Source LS-287, September 2000.

Table 1. Electron beam parameters with the PC-gun beam injected into the linac for Dec. 20, 2001 runs.

Parameter	Uncompressed	Compressed
Beam Energy (MeV)	217 MeV	217
Emittance x (mm mrad)	4.6 after chicane	4.1 after chicane
Emittance y (mm mrad)	4.3 after chicane	4.2 after chicane
Peak Current (A)	120	300
Bunch Length (ps rms)	1.6	0.65
Charge (pC)	450	450
Energy Spread (%)	0.1-0.2	< 0.1

Figure Captions

Fig. 1 A schematic of the diagnostic stations before and between the undulators showing the corrector magnet, YAG:Ce screen actuator, the 45° pick-off mirror, and the filter wheels and cameras.

Fig. 2 A schematic of the flipper mirror ($FM_{n1,2}$) and lens pair ($L_{n1,2}$) transport optics installed at each undulator to transport light to the Oriel imaging spectrometer. There are a total of ten stations.

Fig. 3 A plot of observed, electron-beam spot sizes as a function of z both with and without the 500-nm shortpass filter, which involved mostly OTR and COTR, respectively.

Fig. 4 A plot of the z-dependent intensity scan for the 120-A run in Fig. 3 for the UR (upper) and COTR (lower) data. Noticeable gain and microbunching start in the second half of the undulator string.

Fig. 5 Calculations of the COTR interference patterns for different y-rms sizes of 25, 50, and 100 μm and 0.2% bunching fraction. The OTR pattern is shown as the incoherent case for comparison.

Fig. 6 An example of the imaging spectrometer data showing the x-λ dependence. The horizontal axis is wavelength and the vertical axis is the x-spatial profile. The two clusters are separated by 2.9 nm and 120 μm in wavelength and x space, respectively.

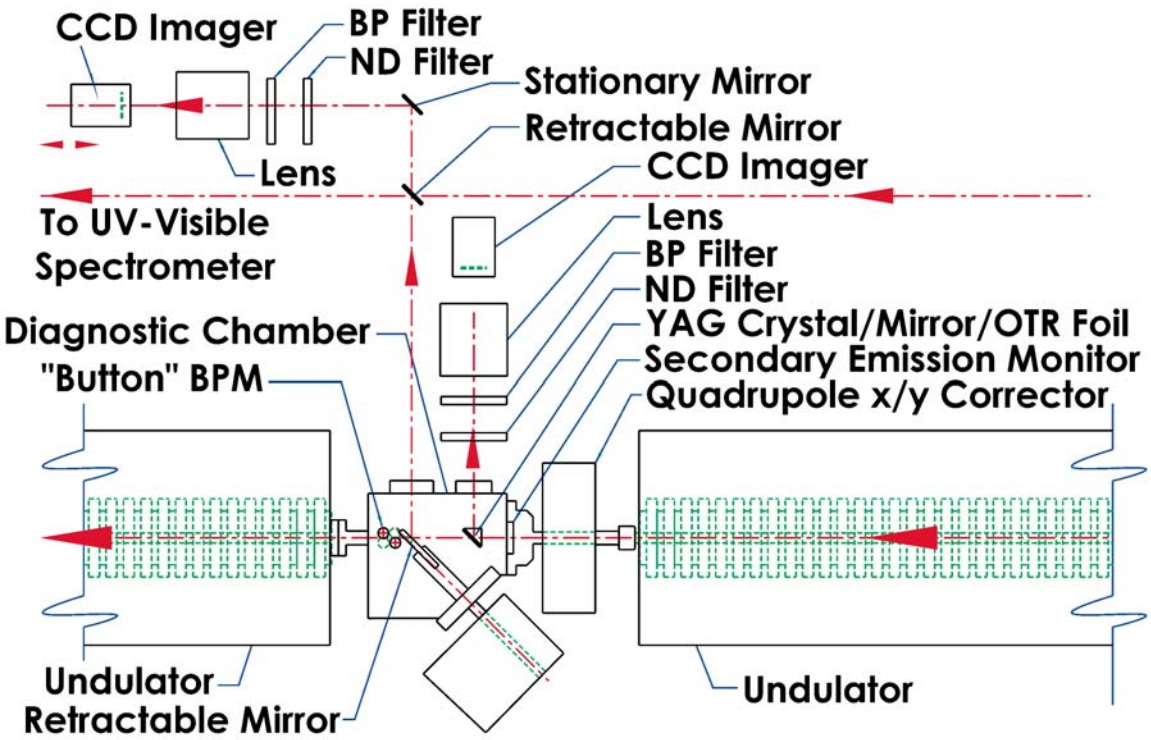
CCD Imager
BP Filter
ND Filter
Stationary Mirror
Retractable Mirror
Lens
CCD Imager
To UV-Visible
Spectrometer
Lens
BP Filter
ND Filter
YAG Crystal/Mirror/OTR Foil
Secondary Emission Monitor
Quadrupole x/y Corrector
Diagnostic Chamber
"Button" BPM
Undulator
Retractable Mirror
Undulator

Fig. 1

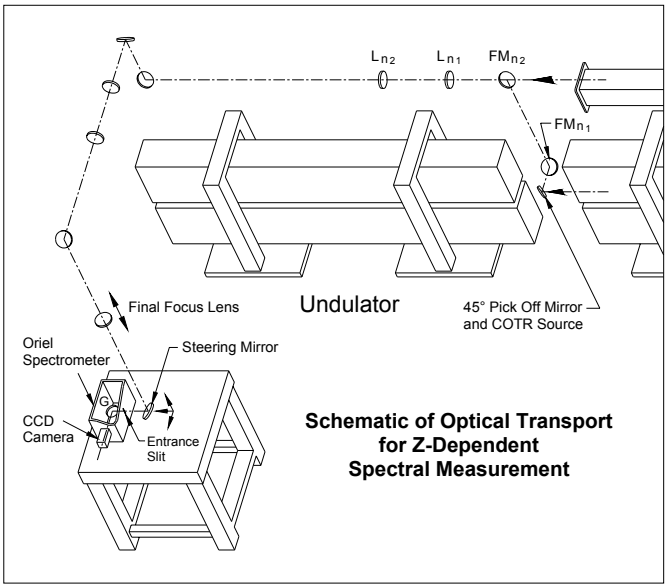
L_{n2}
L_{n1}
FM_{n2}
FM_{n1}
Final Focus Lens
Undulator
45° Pick Off Mirror
and COTR Source
Oriel
Spectrometer
Steering Mirror
CCD
Camera
Entrance
Slit
Schematic of Optical Transport
for Z-Dependent
Spectral Measurement

Fig. 2

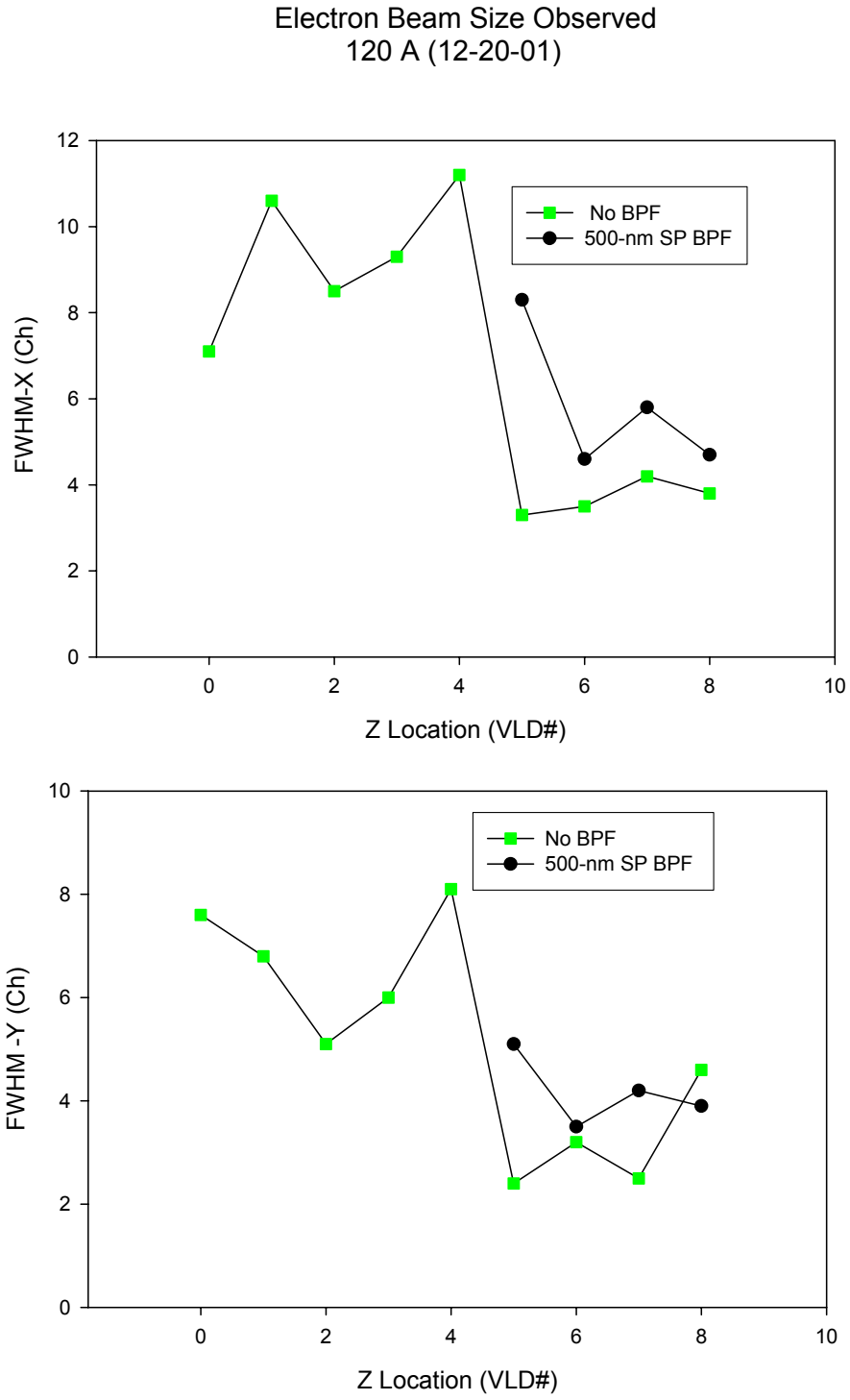
Electron Beam Size Observed
120 A (12-20-01)
FWHM-X (Ch)
Z Location (VLD#)
No BPF
500-nm SP BPF
FWHM -Y (Ch)
Z Location (VLD#)
No BPF
500-nm SP BPF

Fig. 3

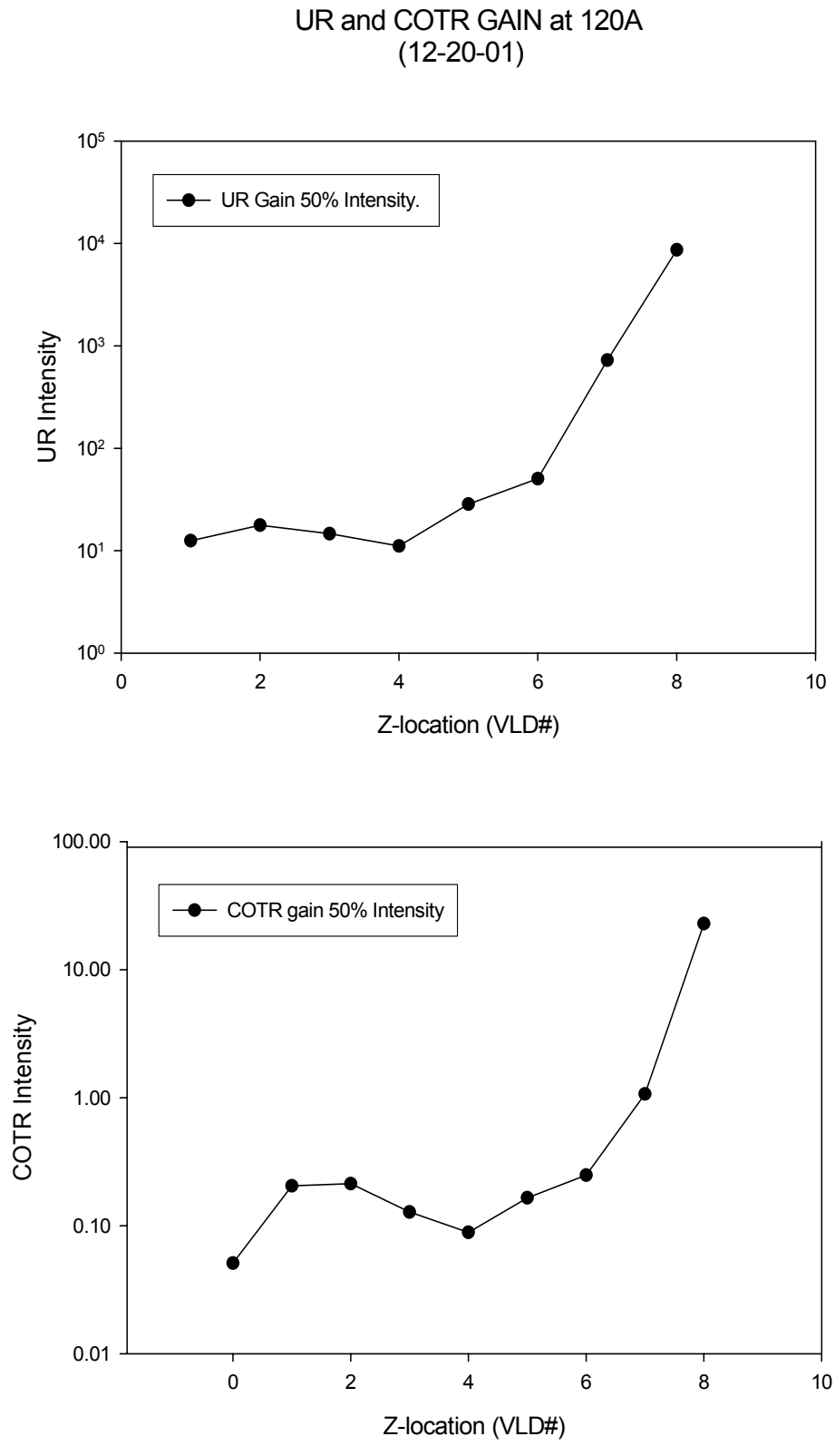
UR and COTR GAIN at 120A
(12-20-01)
UR Gain 50% Intensity.
UR Intensity
Z-location (VLD#)
COTR gain 50% Intensity
COTR Intensity
Z-location (VLD#)

Fig. 4

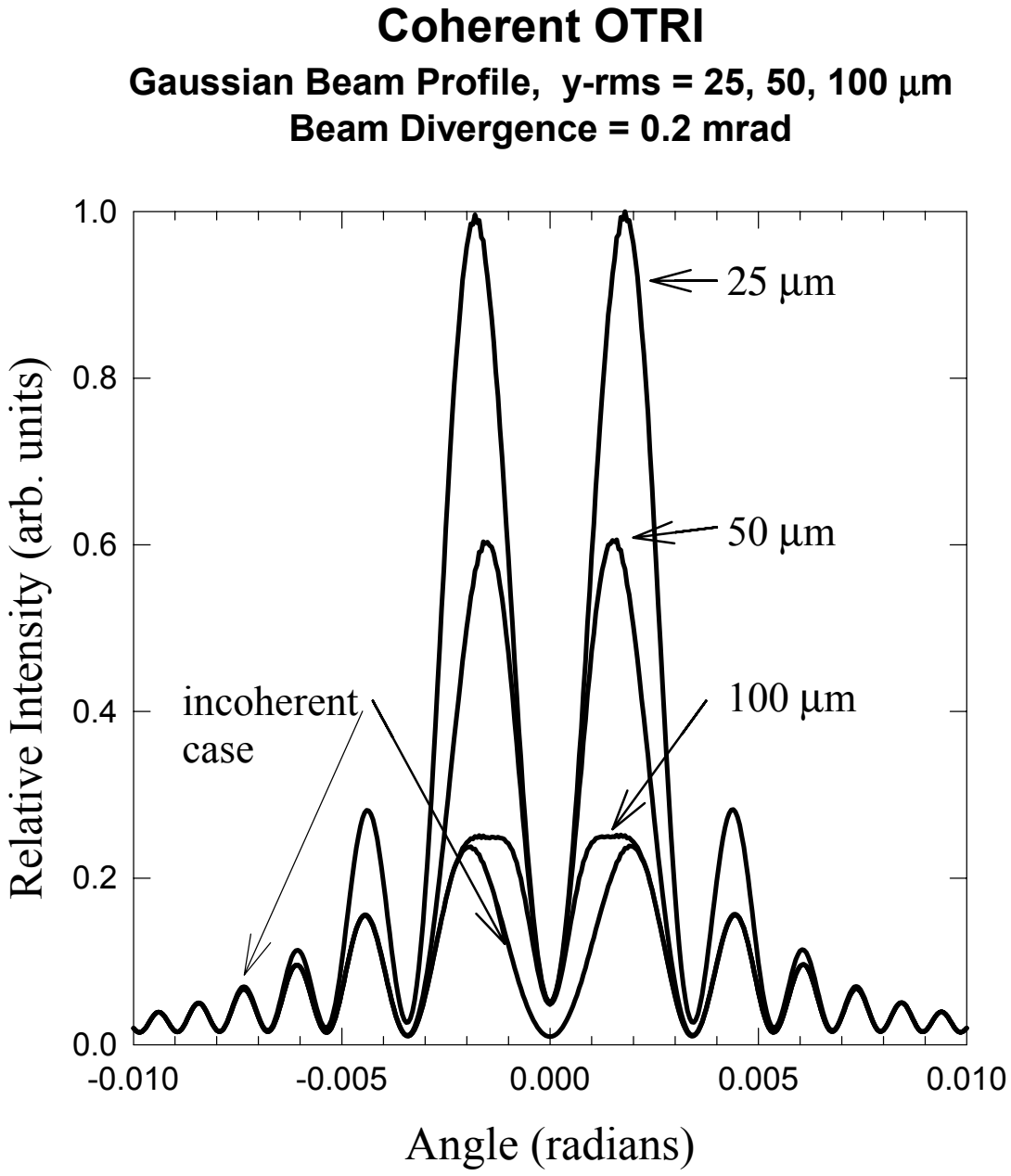
Coherent OTRI
Gaussian Beam Profile, y-rms = 25, 50, 100 μm
Beam Divergence = 0.2 mrad
Relative Intensity (arb. units)
Angle (radians)
1.0
0.8
0.6
0.4
0.2
0.0
-0.010
-0.005
0.000
0.005
0.010
25 μm
50 μm
100 μm
incoherent
case

Fig.5

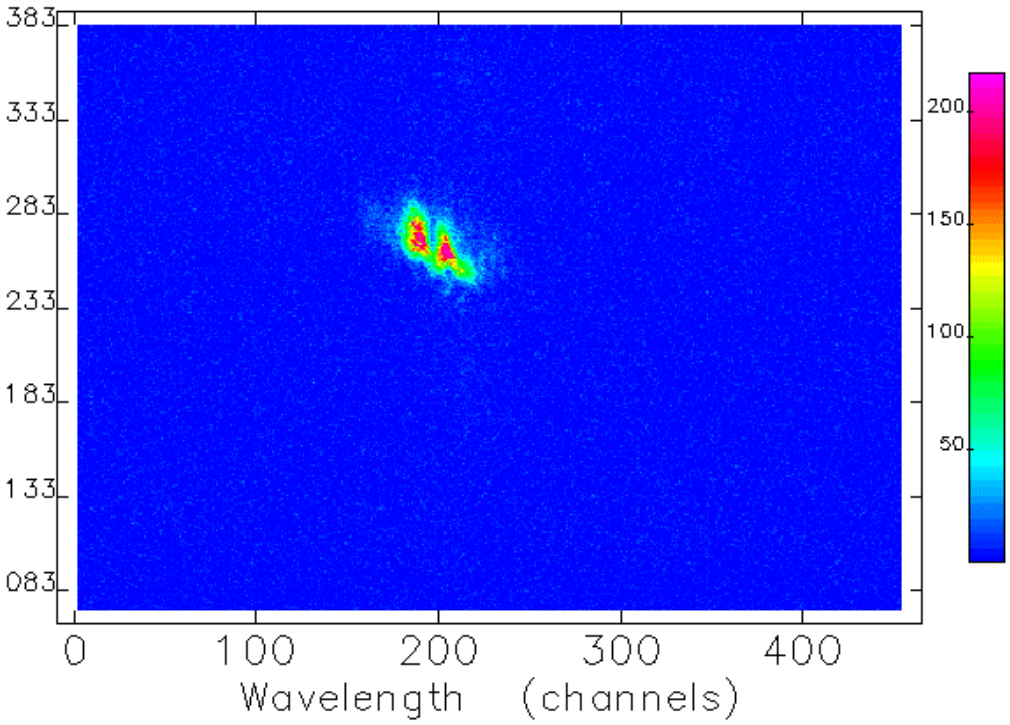
383
333
283
233
183
133
083
0
100
200
300
400
Wavelength (channels)
200
150
100
50

Fig. 6